processes

MDPI

Article

Synthesis of Silver-Decorated Magnetite Nanoparticles Using Self-Assembly Methods

Gye Seok An

Department of Advanced Material Engineering, Kyonggi University, 154-42 Gwanggyosan-ro, Yeongtong-gu, Suwon-si 16227, Republic of Korea; gsmaroan@kyonggi.ac.kr; Tel.: +82-31-249-9763

Abstract: This study investigated the synthesis and functional characteristics of Fe_3O_4@Ag core–shell nanoparticles, focusing on the impact of amino functionalization on their structural and chemical properties. Utilizing self-assembly methods driven by electrostatic interactions, we achieved the effective adsorption of Ag nanoparticles into Fe_3O_4 cores previously modified with silane (APTES) or polymer (PEI) precursors. Our results elucidate how the type of amino precursor affects the surface charge and subsequent adsorption dynamics, revealing that PEI-modified Fe_3O_4 nanoparticles exhibit more substantial Ag nanoparticle adsorption than those modified with APTES. This enhanced adsorption was attributed to the higher density of the amine groups introduced by PEI, which also affected the electrostatic properties of the nanoparticles, as evidenced by their zeta-potential values. Moreover, this study highlighted the role of electrostatic attraction in the self-assembly process, facilitating a controlled synthesis environment that enhances the stability and functionality of nanoparticles for potential biomedical and catalytic applications. This research not only advances our understanding of nanoparticle behavior under different surface chemistries but also demonstrates the importance of surface engineering in optimizing nanoparticle performance for targeted applications.

Keywords: superparamagnetic nanoparticle; self-assembly; magnetite (Fe_3O_4); silver (Ag) nanoparticles; amino functionalization

Citation: An, G.S. Synthesis of Silver-Decorated Magnetite Nanoparticles Using Self-Assembly Methods. *Processes* **2024**, *12*, 1133. https://doi.org/10.3390/pr12061133

Academic Editor: Fabio Carniato

Received: 7 May 2024
Revised: 22 May 2024
Accepted: 28 May 2024
Published: 31 May 2024

1. Introduction

Recent advances in nanotechnology have led to significant progress in the development and application of superparamagnetic nanoparticles, particularly those based on iron oxide (Fe_3O_4) [1–3]. These nanoparticles are pivotal in various biomedical and industrial applications owing to their magnetic properties and surface modifiability. Superparamagnetic iron oxide nanoparticles (SPIONs) are particularly valuable in hyperthermia, drug delivery systems, magnetic resonance imaging contrast enhancement, and as catalysts because of their high magnetic responsiveness and lack of residual magnetism at room temperature [4–7]. This dual functionality allows for external manipulation and prevents particle agglomeration after the magnetic field is removed.

Moreover, the integration of SPIONs with noble metals, such as Pt, Au, and Ag, introduces enhanced functionalities [1,8,9]. AgNPs, known for their antibacterial efficacy and electrical conductivity, are promising candidates for application in wound healing and as conductive materials [10,11]. However, their practical use is often limited by challenges such as recovery after application, prompting research on composite structures such as Fe_3O_4@Ag. This approach not only leverages the easy separation characteristics of Fe_3O_4 but also the distinct antimicrobial properties of silver.

Various synthesis methods have been explored to optimize the physicochemical properties of these nanoparticles. Traditional methods often involve complex procedures that use hazardous chemicals and pose environmental and biological risks. Recent methodologies have focused on the development of Fe_3O_4@Ag nanocomposites using techniques such as hydrothermal synthesis and seed-mediated growth with the aim of enhancing the environmental and biological safety of the synthesis process [12,13].

In particular, the application of core–shell architectures, in which Fe_3O_4 nanoparticles serve as cores, offers a promising strategy for enhancing the functional properties of nanoparticles. The core–shell structure provides a method to fine-tune the interactions of nanoparticles with their environment through controlled surface modifications. Amino-functionalization agents such as (3-aminopropyl)triethoxysilane (APTES) and polyethyleneimine (PEI) have shown considerable promise for facilitating the robust attachment of noble metal nanoparticles to SPIONs, thus enhancing their functionality.

In this study, we explored the synthesis of Fe_3O_4@Ag core–shell nanoparticles using a self-assembly method that capitalizes on the electrostatic interactions between the core and the noble metal. By adjusting the surface chemistry through amino functionalization, we aimed to investigate the adsorption mechanisms and how they influence the stability and functionality of nanoparticles in various applications. This study aimed to investigate the adsorption mechanism of Ag particles based on the structural differences arising from various precursors. This approach not only highlights the potential for tailored nanoparticle design but also aligns with the growing need for sustainable and safe nanomaterials in technology and medicine.

2. Materials and Methods

2.1. Reagents and Materials

High-purity reagents were used in the synthesis and functionalization processes. Ferric chloride hexahydrate ($FeCl_3 \cdot 6H_2O$, 0.01 M; >97%, Sigma-Aldrich, USA), ethylene glycol (EG; >99.5% Samchun Pure Chemical, Republic of Korea), and sodium acetate (NaOAc, >99.5%, Sigma-Aldrich, USA) were used for the synthesis of Fe_3O_4 nanoparticles. For the amino functionalization, (3-aminopropyl)triethoxysilane (APTES, $\geq$99%, Sigma-Aldrich, USA) and polyethyleneimine (PEI, Mw ~25,000, Sigma-Aldrich, USA) were utilized. Silver nitrate ($AgNO_3$, $\geq$99.8%, Sigma-Aldrich, USA), sodium borohydride ($NaBH_4$, 99%, Sigma-Aldrich, USA), sodium hydroxide (NaOH, Duksan, Republic of Korea), and trisodium citrate dihydrate (tSCD, $\geq$99.0%, Sigma-Aldrich, USA) were employed in the silver adsorption experiments.

2.2. Synthesis of Amino-Functionalized Fe_3O_4 Nanoparticles

First, Fe_3O_4 nanoparticles were synthesized using a modified polyol method. A solution containing $FeCl_3 \cdot 6H_2O$ (0.01 M), NaOAc (0.05 M), and EG (100 mL) was prepared in 500 mL of distilled water and mechanically stirred at 70 °C until the color of the solution transitioned from clear to reddish-brown and finally to black, indicating the formation of Fe_3O_4. Upon cooling, the nanoparticles were magnetically separated and washed with ethanol and distilled water to remove any impurities.

Amine functionalization was achieved using two methods. For the first, APTES served as the silane precursor; Fe_3O_4 nanoparticles were ultrasonicated in a mixture of distilled water and ethanol, followed by the addition of 4 mL APTES and stirred in a three-neck round-bottomed flask at 70 °C for 48 h. The particles were cooled, magnetically separated, and washed. In the second method, PEI was used to functionalize the nanoparticles; after ultrasonication with 3 wt% PEI, the mixture was stirred at 80 °C for 18 h, cooled, and the functionalized nanoparticles were washed and stored in distilled water.

2.3. Ag Adsorption Experiments

The Ag adsorption experiments were divided into two types based on the reducing agent used. First, $NaBH_4$ was used as a reducing agent. $AgNO_3$ (0.025 wt%) and tSCD (0.052 wt%) were mixed with 500 mL of distilled water and vigorously stirred at 800 rpm for 10 min, then 14 mL of a $NaBH_4$ (0.005 M) solution was added to the stirred Ag precursor solution to form Ag seeds. A solution consisting of the Fe_3O_4 nanoparticles and 30 mL of distilled water was added to the Ag solution. The suspension was then subjected to mechanical stirring and ultrasonication. The reaction particles were separated using an external magnetic field and washed with distilled water. Second, NaOH was used as a

reducing agent. The same amounts of Ag precursor and tSCD as in the experiment above were mixed in 500 mL of distilled water and mechanically stirred for 10 min, 14 mL of a NaOH (0.005 M) solution was injected into the Ag solution under stirring, then 3 wt% Fe_3O_4 solution was added, reacted using a stirrer, and ultrasonicated for 10 min. The particles were then separated using a strong magnet and washed with distilled water.

2.4. Characterization

The crystal structures of the particles were analyzed using X-ray diffraction (XRD, MiniFlex II, Rigaku, Japan). Subsequently, Fourier-transform infrared spectroscopy (FT-IR, iS50, Thermo Fisher Scientific, USA) was employed to examine the functional groups present on the particle surface after amine functionalization. High-resolution transmission electron microscopy (HR-TEM, Tecnai, FEI, The Netherlands) and energy-dispersive spectroscopy (EDS, EDAX detector (DPP-II), USA) were used to obtain detailed information about the particles. Surface charge analysis was conducted to evaluate the zeta potential (Zetasizer Nano ZS, Malvern Inc., USA) before and after Ag adsorption using dynamic light scattering (DLS) mode in zeta potential.

3. Results and Discussion

The FT-IR spectra of the nanoparticles were analyzed post-synthesis and functionalization to determine surface chemistry changes, as depicted in Figure 1. All spectra prominently featured a peak at 590.41 cm^{-1}, characteristic of the Fe–O bond, indicating the integrity of the iron oxide structure across all samples. For the as-prepared Fe_3O_4 nanoparticles, the peaks at 1645.56 and 3450.17 cm^{-1} were attributed to the bending and stretching vibrations of the O–H bond, respectively, confirming the presence of surface hydroxyl groups. These groups are critical for the subsequent surface modifications.

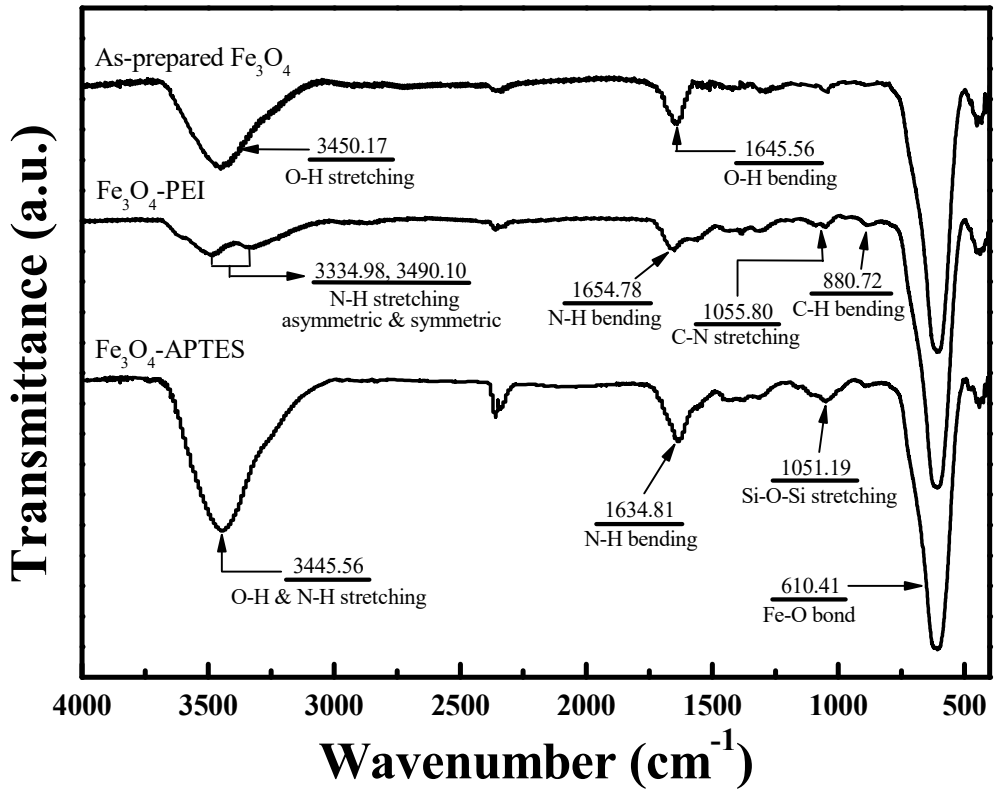

Figure 1. FT-IR spectra of the as-prepared Fe_3O_4, PEI-treated Fe_3O_4, and APTES-treated Fe_3O_4.

Post-functionalization with PEI, a polymer precursor, led to the emergence of several new peaks: C–H bending at 880.72 cm^{-1} and C–N stretching at 1055.80 cm^{-1}, suggesting the formation of a polymer layer enveloping the nanoparticle surface [14]. Notably, a peak

at 1654.78 cm^{-1} indicated the N–H bending mode of terminal amine groups, with additional peaks at 3334.98 cm and 3580.10 cm^{-1} corresponding to symmetric and asymmetric N–H stretching vibrations, respectively. Conversely, the FT-IR spectrum of the APTES-modified Fe_3O_4 displayed different characteristics. A distinct peak at 1083.91 cm^{-1}, representative of Si-O-Si stretching, confirmed the formation of silane bonds, likely due to a condensation reaction with the surface hydroxyl groups. N–H bending vibration was observed at 1634.81 cm^{-1}, with significant intensity compared to that of the PEI-treated samples [15]. A composite peak at 3445.56 cm^{-1}, merging the O–H stretching and N–H stretching vibrations, suggested an overlap of these functional groups due to the dense packing of APTES on the nanoparticle surface.

The successful attachment of amino groups to the nanoparticle surface was evident from the N–H vibration peaks in the spectra of both the PEI- and APTES-modified samples. However, the distinct spectral features following the PEI and APTES treatments highlight the different chemical environments created by these precursors. The decrease in the intensity of the O–H stretching peak post-PEI treatment and the emergence of Si-O-Si stretching vibrations post-APTES treatment underscore the transformative impact of these functionalizations on nanoparticle surface chemistry. These spectral findings not only confirm the successful modification of Fe_3O_4 nanoparticles but also illustrate how different precursors influence the nature of surface functional groups, guiding their potential applications in targeted technological fields.

Zeta-potential measurements were conducted to assess the surface charge characteristics and dispersion stabilities of the as-prepared and amino-functionalized Fe_3O_4 nanoparticles, as illustrated in Figure 2. The as-prepared Fe_3O_4 nanoparticles exhibited a negative surface charge of −20.43 mV, indicating the inherent surface chemistry prior to modification. Upon amino functionalization, a significant shift in the zeta potential toward positive values was observed, reflecting changes in surface chemistry. Specifically, the zeta potential increased to +30.63 mV for the PEI-treated nanoparticles and +24.42 mV for the APTES-treated nanoparticles. This increase can be attributed to the nature of the functional groups introduced during amino functionalization. PEI, a polymeric precursor, formed a network of carbon chains and terminal amine groups that encapsulated the nanoparticle surface. This dense packing of amine groups increases the overall surface charge, explaining the higher zeta potential observed with PEI than with APTES. In contrast, APTES functionalization involved fewer hydroxyl group interactions and formed a silane layer via condensation, leading to a moderately positive surface charge. Furthermore, the polydispersity index (PDI), which is an indicator of particle dispersion in colloidal systems, displayed trends distinct from those of the surface charge. The lowest PDI value (0.18) was observed for PEI-functionalized Fe_3O_4, indicating superior particle dispersion. This contrasts with the as-prepared Fe_3O_4 and APTES-functionalized nanoparticles, which had PDI values of 0.20 and 0.31, respectively. The relatively high PDI of the APTES-functionalized nanoparticles suggests potential particle aggregation during the SiO condensation reaction, which may reduce the dispersion quality. Conversely, the enhanced dispersion stability in the PEI-functionalized nanoparticles is likely due to stronger electrostatic repulsion among the particles as a result of the higher positive surface charge (Figure 3).

When the as-prepared Fe_3O_4 was amino-functionalized, the surface charge became positive because of the amine groups on the surface. In contrast, Ag nanoparticles obtained using $AgNO_3$ as a precursor had a negative charge owing to citrate functionalization of the surface, which occured as a result of the tSCD used during the synthesis process. As a result, Fe_3O_4@Ag nanoparticles were formed with Ag nanoparticles decorating the surface of the Fe_3O_4 nanoparticles.

Decorated Ag nanoparticles were synthesized using different reduction reactions depending on the type of reducing agent used. When $NaBH_4$ was used as the reducing agent, the reaction proceeded according to the formula represented by Equation (1). In this reaction, $AgNO_3$ and $NaBH_4$ were reacted to yield a 1:1 ratio of $NaNO_3$ to Ag. However, when NaOH is used as the reducing agent, as indicated in Equations (2) and (3), the

reaction between $AgNO_3$ and NaOH results in the formation of Ag_2O and $NaNO_3$ [16]. Subsequently, Ag_2O underwent ionization in an aqueous solution. Following this, as indicated in Equation (4), Ag_+ undergoes a redox reaction with the electrons from tSCD, resulting in the formation of Ag and the ionization of Na.

$$2AgNO_3 + 2NaBH_4 \rightarrow B_2H_6 + H_2 \uparrow + 2Ag^0 + 2NaNO_3 \quad (1)$$

$$2AgNO_3 + 2NaOH \rightarrow Ag_2O\ (s) + 2NaNO_3 + H_2O\ (l) \quad (2)$$

$$Ag_2O + H_2O + 2e^- \rightarrow 2Ag + 2OH^\bullet \quad (3)$$

$$4Ag^+ + C_6H_5O_7Na_3 + 2H_2O \rightarrow 4Ag^0 + C_6H_5O_7H_3 + 3Na^+ + H^+ + O_2 \uparrow \quad (4)$$

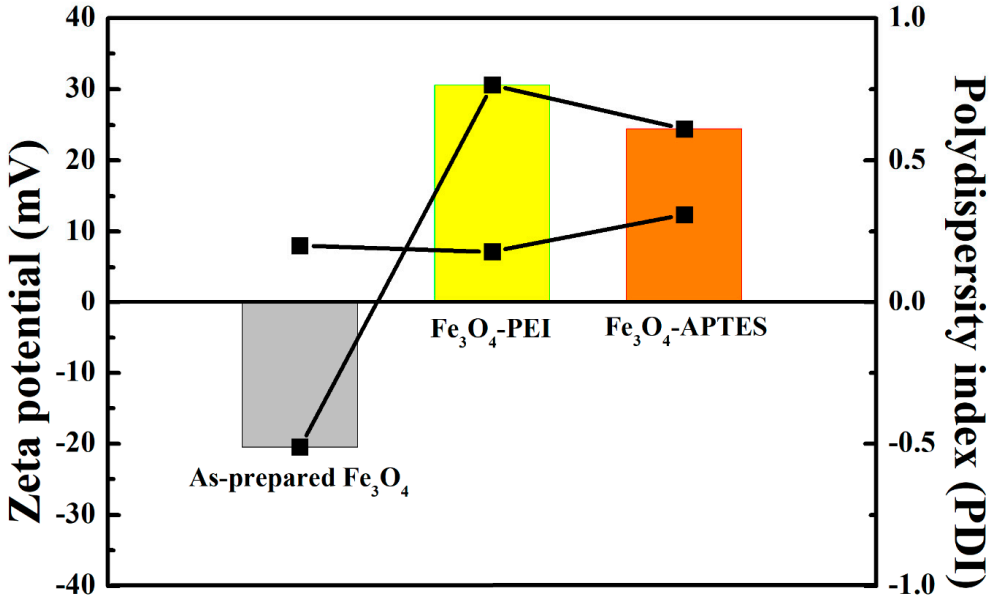

Figure 2. Surface charge and dispersion characteristics of as-prepared Fe_3O_4 and amino-functionalized Fe_3O_4.

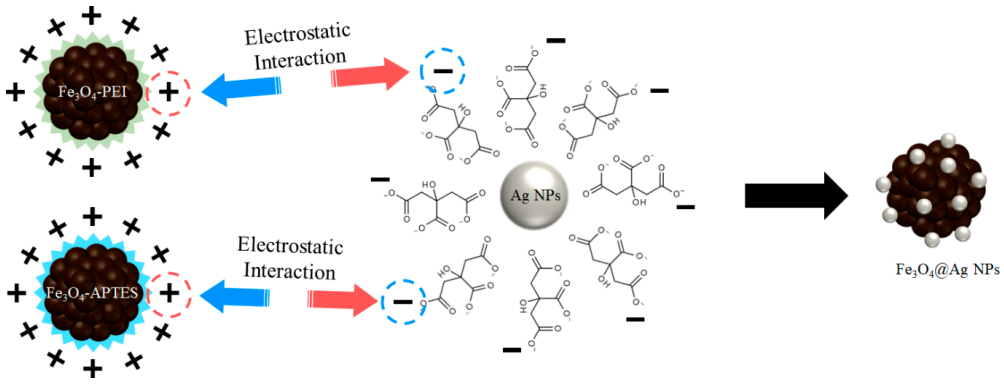

Figure 3. Scheme of Fe_3O_4@Ag nanoparticle synthesis mechanism.

Figure 4 shows the transmission electron microscopy (TEM) and selected area electron diffraction (SAED) patterns of Fe_3O_4@Ag nanoparticles synthesized using different amino-functionalization precursors, specifically PEI and APTES with $NaBH_4$ (reducing agent). The TEM images confirmed the presence of silver nanoparticles adsorbed in the surfaces of both the PEI- and APTES-treated Fe_3O_4 nanoparticles. The size of the adsorbed Ag particles ranged from 11 nm to 62 nm. Notably, a higher quantity of Ag nanoparticles was adsorbed into the PEI-modified Fe_3O_4 nanoparticles than onto those modified with

APTES. High-resolution TEM (HR-TEM) further delineated the microstructural details of the adsorbed AgNPs. The images displayed distinct striped patterns with lattice spacings of 1.99 and 1.42 Å, correlating with the (200) and (220) crystallographic planes of Ag, respectively [17]. These observations were substantiated by SAED pattern analysis, in which the diffraction patterns corresponding to the (200) and (220) planes of Ag were distinctly visible, confirming the successful adsorption of Ag nanoparticles following amine functionalization. The enhanced adsorption observed in the PEI-modified samples was attributed to the higher density of amine groups available for binding the Ag nanoparticles.

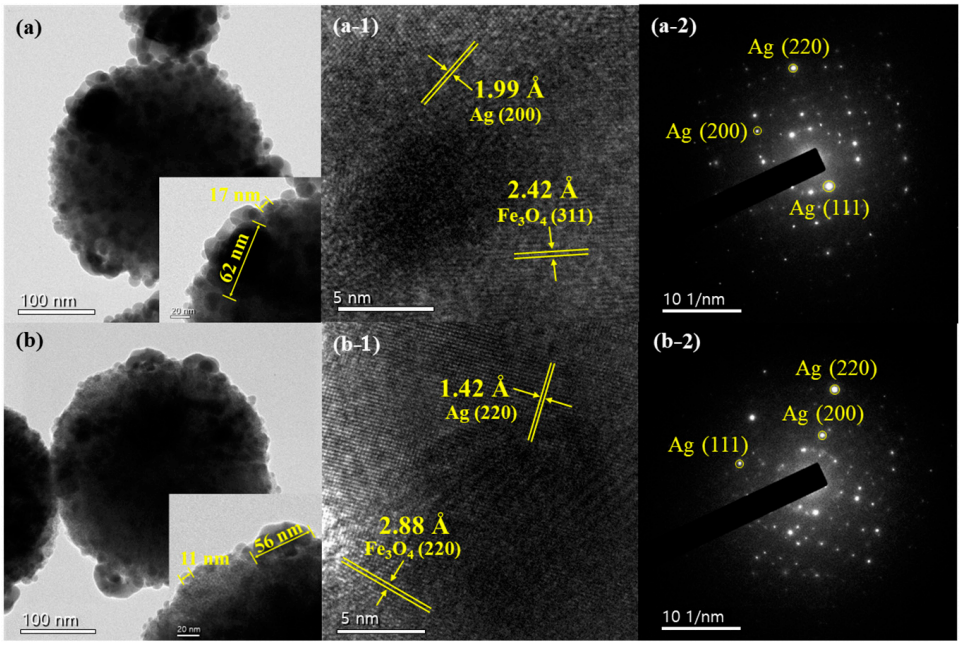

Figure 4. High-resolution TEM images and selected area electron diffraction (SAED) patterns of Ag adsorption: (**a**) PEI-treated Fe_3O_4, (**b**) APTES-treated Fe_3O_4 nanoparticles.

The adsorption morphologies and microstructures of the nanoparticles were characterized using high-resolution TEM (Figure 5). This analysis revealed significant differences in the adsorption efficiencies of the nanoparticles reduced with NaBH4 and those reduced with NaOH with PEI as an amine precursor. When $NaBH_4$ was used as the reducing agent, extensive adsorption of Ag nanoparticles was evident, suggesting effective nucleation and growth on the Fe_3O_4 surface. Conversely, minimal Ag nanoparticle adsorption was observed when NaOH was used as the reducing agent. This disparity was likely due to the different mechanisms of silver ion reduction by these agents. $NaBH_4$ rapidly reduces $AgNO_3$ to metallic Ag, facilitating immediate nanoparticle formation and adsorption. In contrast, NaOH induces the preliminary formation of Ag_2O, which subsequently reacts with tri-sodium citrate dihydrate (tSCD) to slowly produce Ag nanoparticles.

Microstructural analysis under high-resolution TEM revealed lattice patterns with spacings of 1.96 and 2.82 Å, corresponding to the (200) plane of Ag and the (220) plane of Fe_3O_4, respectively. This finding indicates the limited adsorption of Ag nanoparticles, presumably owing to the slower reaction kinetics associated with the NaOH reduction pathway. The reduced Ag particle formation rate during the allotted reaction time resulted in less adsorption into the Fe_3O_4 surface when NaOH was used compared to $NaBH_4$. These findings collectively highlight the influence of amino functionalization and the choice of reducing agent on the adsorption and microstructural characteristics of Fe_3O_4@Ag nanoparticles, offering insights into optimizing nanoparticle synthesis to enhance functional properties.

The XRD patterns displayed in Figure 6 elucidate the crystalline structures of the Fe_3O_4@Ag nanoparticles synthesized using various precursors and reducing agents. Figure 6a confirms the presence of distinct diffraction peaks characteristic of Fe_3O_4 across all the

samples, regardless of the precursor used. These peaks appear at 2θ values of 30.1°, 35.5°, 37.1°, 43.1°, 53.5°, 57.0°, 62.7°, 71.1°, and 74.1°, corresponding to the (220), (311), (222), (400), (422), (511), (440), (620), and (533) planes, respectively, which are indexed to the standard JCPDS 65-3107 [18]. This pattern confirmed the retention of the cubic inverse spinel structure of Fe_3O_4 in the synthesized nanoparticles.

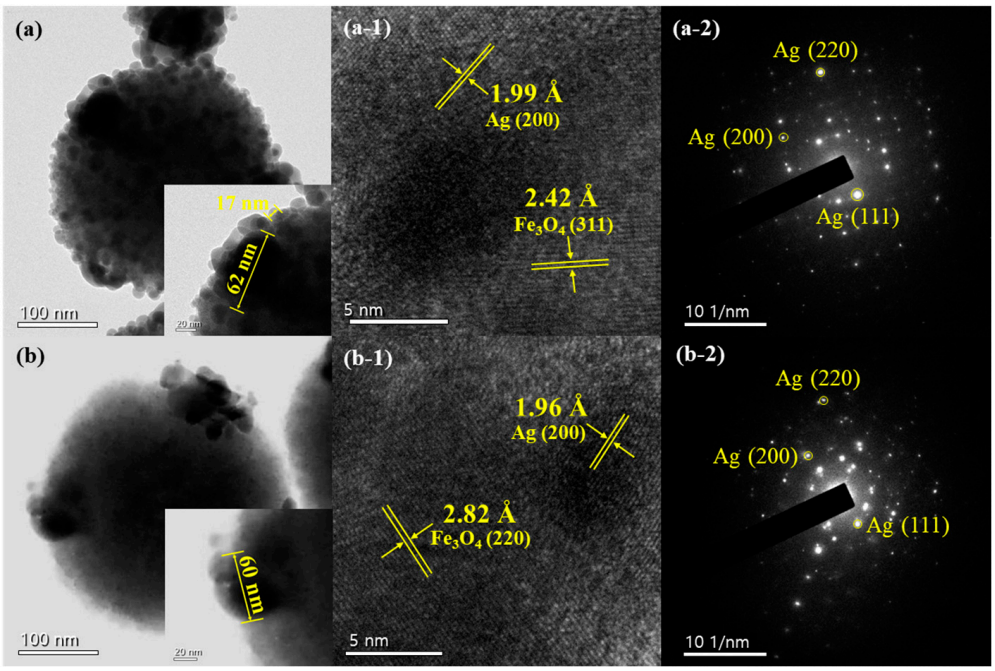

Figure 5. High-resolution TEM images and SAED patterns of Ag adsorption: (**a**) $NaBH_4$ used, (**b**) NaOH used Fe_3O_4@Ag nanoparticles.

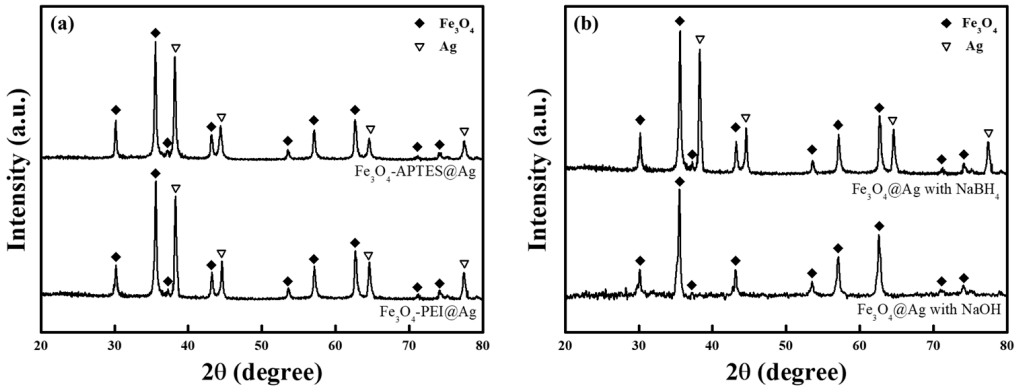

Figure 6. X-ray diffraction (XRD) patterns of Fe_3O_4@Ag (**a**) depending on the amino precursor (PEI vs. APTES) under $NaBH_4$ condition and (**b**) depending on the reductant ($NaBH_4$ vs. NaOH) under PEI condition.

Simultaneously, the Ag diffraction pattern is evident in all samples, appearing at 2θ values of 38.3°, 44.5°, 64.8°, and 77.5°, associated with the crystal planes (111), (200), (220), and (311), respectively (JCPDS 04-0783) [16]. These results are consistent with the microstructural analysis previously conducted using high-resolution TEM, further validating the cubic face-centered cubic crystalline structure of the Ag nanoparticles. The pronounced sharp peaks of both Fe_3O_4 and Ag indicate the high crystallinity of these materials. The comparable peak intensities of the Fe_3O_4-PEI@Ag and Fe_3O_4-APTES@Ag samples indicated that the amino-functionalization process did not adversely affect the crystalline properties of the nanoparticles. Moreover, the absence of any extraneous diffrac-

tion peaks confirmed that the Ag nanoparticles were synthesized without any oxidation, thus confirming the integrity and purity of the post-synthesis nanoparticles. This confirms no oxidation or structural deformation during the adsorption process on the Fe_3O_4 surface.

However, as shown in Figure 6b, a deviation was observed when NaOH (with PEI) was used as the reducing agent. In these instances, only the diffraction peaks of Fe_3O_4 are discernible, with no apparent Ag diffraction peaks. This suggests that the Ag nanoparticles adsorbed into the Fe_3O_4 surface were insufficient in quantity or size to be detected by XRD, likely because of the relatively weaker reducing capabilities of NaOH compared to $NaBH_4$. This weaker reduction capability may have impeded the adequate growth of Ag nuclei to yield detectable diffraction patterns, suggesting limitations in the use of NaOH for effective Ag nanoparticle synthesis on Fe_3O_4 substrates.

The Ag adsorption mechanism of the Fe_3O_4 nanoparticles according to the precursor and reducing agent was investigated through chemical composition analysis using EDS based on TEM (Figure 7). Here, when Fe-K, O-K, and Ag-L are qualitatively analyzed through EDS, X-rays such as K, L, M, N, and O are generated in series for each element, and the acceleration voltage and EDS energy range, if the conditions are properly set so that X-rays of each line can be sufficiently generated, can be used to check whether these series lines are properly generated and serve as a basis for trusting the peak of that element. Potential elemental mapping was performed for Fe-K, O-K, and Ag-L. For the PEI-modified sample named Fe_3O_4-PEI@Ag, and revealed the existence of particles with a core diameter of approximately 306 nm, primarily composed of Fe and O. Furthermore, the Ag-L element distribution demonstrated a consistent dispersion of Ag across an area measuring approximately 327 nm. This distribution surrounds regions with a certain mass corresponding to the luminous areas inferred to be Ag nanoparticles, as observed in Figure 7a-1. This analysis confirms the presence of larger Ag nanoparticles within some agglomerated regions. A perceptible size difference of approximately 21 nm was confirmed between the core and Ag-L images, suggesting the adsorption of Ag nanoparticles into the surface of the core particles with an estimated thickness of approximately 10 nm.

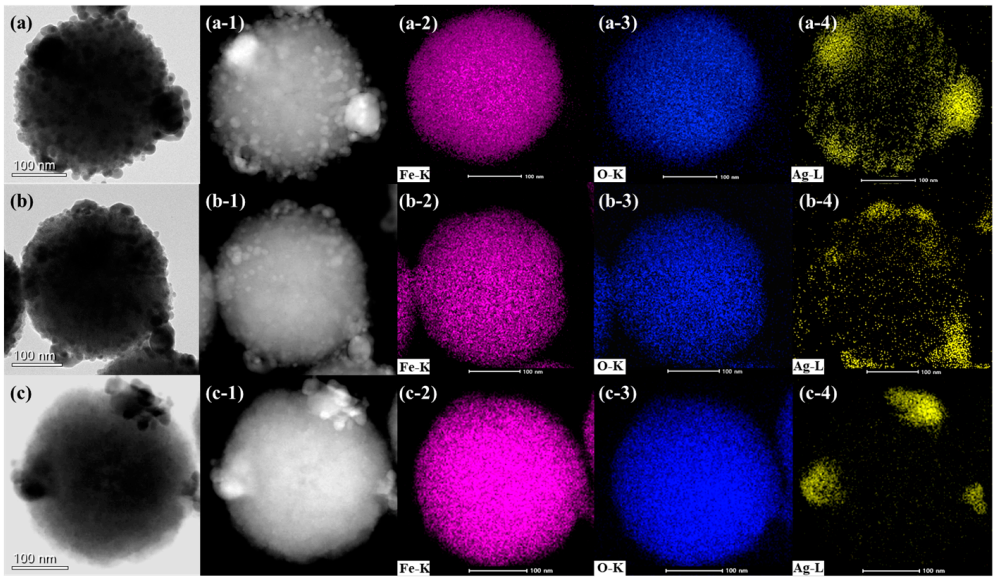

Figure 7. TEM and EDS mapping images of Ag adsorption: (**a**) PEI-modified Fe_3O_4 with $NaBH_4$, (**b**) APTES-modified Fe_3O_4 $NaBH_4$, (**c**) PEI-modified Fe_3O_4 using NaOH as reducing agent.

In the case of the Fe_3O_4 particles subjected to surface modification with APTES, elemental mapping revealed Fe-K and O-K with diameters of approximately 314 nm, whereas Ag-L had a diameter of approximately 318 nm (Figure 7b). This resulted in a relatively small size difference of approximately 4 nm, suggesting that Ag was adsorbed into the surface with an estimated thickness of approximately 2 nm around. Evaluation

of the Ag mapping image indicated an overall uniform distribution. However, compared to the PEI-modified Fe_3O_4 sample, a relatively lower degree of distribution was observed. The Ag content adsorbed in the amino-functionalized Fe_3O_4 surface was compared by referring to the atomic and weight percentages, as shown in Table 1. It was confirmed that PEI-modified Fe_3O_4 and APTES-modified Fe_3O_4 contained 5.88 at% and 3.24 at% of Ag nanoparticles, respectively. In addition, the weight % of Ag nanoparticles adsorbed in PEI-modified Fe_3O_4 was the highest at 16.63 wt%, indicating that the Ag content of the sample was the highest. Consequently, while Ag nanoparticles adsorbed uniformly after amine functionalization, the PEI modification resulted in a higher adsorption rate.

Table 1. Chemical concentration of Fe_3O_4@Ag based on the type of precursor and reducing agent.

Samples	Atomics (Atomic %)			Weights (Weight %)		
	Fe	O	Ag	Fe	O	Ag
Fe_3O_4-PEI@Ag	42.00	52.12	5.88	61.50	21.87	16.63
Fe_3O_4-APTES@Ag	45.44	51.32	3.24	68.42	22.14	9.44
Fe_3O_4-PEI@Ag with NaOH	30.52	68.19	1.29	58.09	37.19	4.72

According to the zeta-potential results of amino-functionalized Fe_3O_4, it is evident that the use of PEI results in a higher charge and more amine groups are formed on the surface. Consequently, it was concluded that Ag nanoparticles could be most efficiently adsorbed into the particle surface when the polymer precursor was capable of generating a larger number of amine groups on the surface via amine functionalization.

Elemental mapping analysis of the Fe_3O_4-PEI@Ag particles, synthesized using NaOH as the reducing agent, showed that the Fe and O constituents of the core displayed a diameter of approximately 307 nm. In the Ag-L element mapping image, in contrast to the previous two samples, Ag was concentrated at three distinct locations. This observation supports the brightly illuminated areas corresponding to the Ag nanoparticles in the three specific regions shown in Figure 7c-1, signifying that aside from the larger Ag nanoparticles, no additional Ag nanoparticles were adsorbed into the particle surface.

The zeta potential was analyzed to investigate the changes in the surface charge and dispersion after Ag nanoparticle adsorption (Table 2). The surface charge of the nanoparticles shifted from positive to negative after Ag adsorption for both the PEI and APTES modifications. Specifically, Fe_3O_4-PEI@Ag indicated a surface charge of -20.39 mV, while Fe_3O_4-APTES@Ag showed a surface charge of -9.02 mV.

Table 2. Surface charge and dispersion in the colloidal suspensions of Fe_3O_4-PEI@Ag, and Fe_3O_4-APTES@Ag.

Sample	Zeta Potential (mV)	Polydispersity Index
Fe_3O_4-PEI@Ag ($NaBH_4$)	-20.39 ± 0.56	0.22 ± 0.015
Fe_3O_4-APTES@Ag ($NaBH_4$)	-9.02 ± 0.24	0.38 ± 0.135
Fe_3O_4-PEI@Ag (NaOH)	26.91 ± 1.03	0.21 ± 0.014

In contrast, when NaOH was used as the reducing agent for Fe_3O_4-PEI@Ag, the surface charge was measured at +26.91 mV. This can be considered a basis for supplementing the elemental analysis results. Considering the charge of the PEI-modified Fe_3O_4 nanoparticles was +30.63 mV suggests that the number of Ag nanoparticles was minimal when NaOH was used as the reducing agent, indicating that the charge of the Ag nanoparticles had an insignificant impact on the surface charge.

In the colloidal state, an electric double layer is formed on the particle surface. A stern layer is formed directly on the particle surface, topped by a diffusion layer. The concentration of the adsorbed Ag decreased as the distance from the Fe_3O_4 surface increased. Based

on this hypothesis, we conclude that the PEI-modified Fe_3O_4@Ag nanoparticles show the most negative charge, resulting in the adsorption of the highest number of Ag nanoparticles (Figure 8).

The magnetic properties of the as-prepared Fe_3O_4, Fe_3O_4-PEI@Ag, and Fe_3O_4-APTES@Ag nanoparticles were analyzed using a vibrating-sample magnetometer. Coercive force and residual magnetization were not observed in any of the particles. The as-prepared Fe_3O_4 nanoparticles exhibited the highest saturation magnetization (121.6 emu/g). It was observed that Fe_3O_4-PEI@Ag and Fe_3O_4-APTES@Ag had saturation magnetization values of 72.5 emu/g and 78.4 emu/g, respectively. However, the saturation magnetization was higher when APTES was used than when amine functionalization was performed with PEI.

The hysteresis loop shows a significant decrease in saturation magnetization after Ag adsorption. This is a phenomenon in which the magnetic properties depend on the mass, and the saturation magnetization decreases significantly as the mass of the Fe_3O_4 nanoparticles increases due to Ag adsorption.

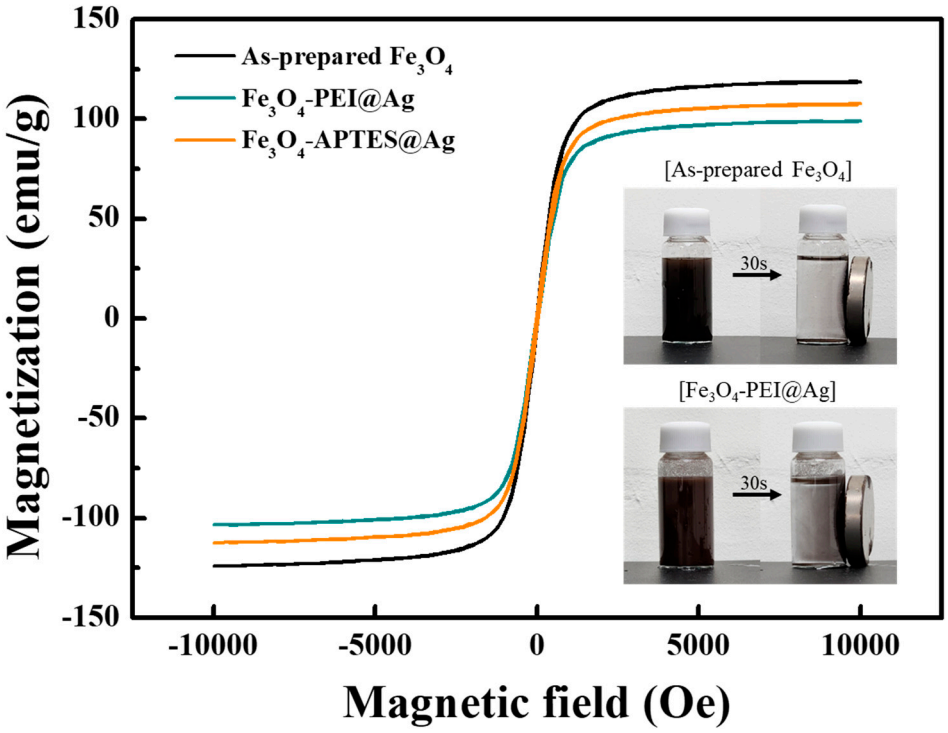

Figure 8. Hysteresis loop of as-prepared Fe_3O_4, Fe_3O_4-PEI@Ag, and Fe_3O_4-APTES@Ag.

4. Conclusions

In this study, Fe_3O_4@Ag nanoparticles were synthesized by the adsorption of Ag nanoparticles into the surfaces of Fe_3O_4 nanoparticles, which were surface-modified by amine functionalization. This synthetic method utilizes a self-assembly approach that harnesses electrostatic attraction. Surface charge analysis provided compelling evidence that the amino-functionalized Fe_3O_4 nanoparticles showed a higher positive surface charge when the polymer precursor was used.

We comprehensively investigated the Ag adsorption mechanism, focusing on the effects of different precursors and reducing agents. TEM was performed to investigate the Ag adsorption patterns relative to the precursors used. The Ag nanoparticles showed uniform adsorption into the particle surface for both the polymer and silane precursors. Particle crystallinity analyses confirmed the crystalline nature of both the Fe_3O_4 and Ag nanoparticles. Elemental analysis was performed to compare the compositions, revealing that the polymer precursor resulted in the most uniform Ag adsorption in the surface, whereas the use of NaOH as the reducing agent led to the least Ag adsorption in the surface.

Funding: This work was supported by Kyonggi University Research Grant 2021.

Data Availability Statement: All data used to support the findings of this study are included in this article.

Conflicts of Interest: The author declares no conflicts of interest.

References

1. Saraçoğlu, M.; Mansoor, M.; Bakırdöven, U.; Arpalı, H.; Gezici, U.O.; Timur, S. Challenging the frontiers of superparamagnetism through strain engineering: DFT investigation and co-precipitation synthesis of large aggregated Fe_3O_4 (magnetite) powder. *J. Alloys Compd.* **2023**, *968*, 171895. [CrossRef]
2. Yew, Y.P.; Shameli, K.; Miyake, M.; Ahmad Khairudin, N.B.B.; Mohamad, S.E.B.; Naiki, T.; Lee, K.X. Green biosynthesis of superparamagnetic magnetite Fe_3O_4 nanoparticles and biomedical applications in targeted anticancer drug delivery system: A review. *Arab. J. Chem.* **2020**, *13*, 2287–2308. [CrossRef]
3. Chen, X.; Zhang, Y.; Zhao, Y.; Wang, S.; Liu, L.; Xu, W.; Guo, Z.; Wang, S.; Liu, Y.; Zhang, J. Encapsulating Pt Nanoparticles through Transforming Fe_3O_4 into MIL-100(Fe) for Well-Defined Fe_3O_4@Pt@MIL-100(Fe) Core-Shell Heterostructures with Promoting Catalytic Activity. *Inorg. Chem.* **2019**, *58*, 12433–12440. [CrossRef] [PubMed]
4. Ishibe, T.; Maeda, Y.; Terada, T.; Naruse, N.; Mera, Y.; Kobayashi, E.; Nakamura, Y. Resistive switching memory performance in oxide hetero-nanocrystals with well-controlled interfaces. *Sci. Technol. Adv. Mater.* **2020**, *21*, 195–204. [CrossRef] [PubMed]
5. Wu, N.; Liu, C.; Xu, D.; Liu, J.; Liu, W.; Shao, Q.; Guo, Z. Enhanced Electromagnetic Wave Absorption of Three-Dimensional Porous Fe_3O_4/C Composite Flowers. *ACS Sustain. Chem. Eng.* **2018**, *6*, 12471–12480. [CrossRef]
6. Yazdanpanah, A.; Ghaffari, M.; Ahmadi, Z.; Abrishamkar, A.B.; Sattarzadeh, S.; Ramedani, A.; Arabyazdi, S.; Moztarzadeh, F. Threatening sarcoma with combinational therapies: Magnetic hyperthermia using nanoparticles. *Nano Select.* **2023**, *4*, 353–367. [CrossRef]
7. Eskandani, M.; Derakhshankhah, H.; Jahanban-Esfahlan, R.; Jaymand, M. Folate-conjugated pH- and redox-responsive magnetic hydrogel based on tragacanth gum for "smart" chemo/hyperthermia treatment of cancerous cells. *J. Drug Del. Sci. Technol.* **2023**, *84*, 104449. [CrossRef]
8. Hur, J.U.; Shin, J.R.; Han, J.S.; Kim, Y.H.; An, G.S. Self-assembled core-shell Fe_3O_4-Pt nanoparticles via silylation/polymerization-based amino-functionalization. *Colloid Interface Sci. Commun.* **2022**, *50*, 100655. [CrossRef]
9. Yeneayehu, K.; Senbeta, T.; Mesfin, B. Enhancement of the optical response of core-shell nanoparticles. *Phys. E Low-Dimens. Syst. Nanostruct.* **2021**, *134*, 114822. [CrossRef]
10. Lv, H.; Cui, S.; Yang, Q.; Song, X.; Wang, D.; Hu, J.; Zhou, Y.; Liu, Y. AgNPs-incorporated nanofiber mats: Relationship between AgNPs size/content, silver release, cytotoxicity, and antibacterial activity. *Mater. Sci. Eng. C* **2021**, *118*, 111331. [CrossRef] [PubMed]
11. Krishna, K.; Harisha, K.S.; Neelakandan, R.; Sangappa, Y. Fabrication and conductivity study of silver nanoparticles loaded polyvinyl alcohol (PVA-AgNPs) nanofibers. *Mater. Today Proc.* **2021**, *42*, 515–520. [CrossRef]
12. Hajalilou, A.; Ferreira, L.P.; Jorge, M.E.M.; Reis, C.P.; Cruz, M.M. Superparamagnetic Ag-Fe_3O_4 composites nanoparticles for magnetic fluid hyperthermia. *J. Magn. Magn. Mater.* **2021**, *537*, 168242. [CrossRef]
13. Song, Y.; Chen, J.; Yang, X.; Zhang, D.; Zou, Y.; Ni, D.; Ye, J.; Yu, Z.; Chen, Q.; Jin, S.; et al. Fabrication of Fe_3O_4@Ag magnetic nanoparticles for highly active SERS enhancement and paraquat detection. *Microchem. J.* **2022**, *173*, 107019. [CrossRef]
14. Han, J.; An, G.S. Core-shell-type Fe_3O_4@carbon nanoparticles and their fabrication using silanic/polymeric amino functionalization. *Ceram. Inter.* **2021**, *47*, 28669–28674. [CrossRef]
15. Shahin, R.; Yousefi, M.; Ziyadi, H.; Bikhof, M.; Hekmati, M. pH-Responsive and magnetic Fe_3O_4@ UiO-66-NH_2@ PEI nanocomposite as drug nanocarrier: Loading and release study of Imatinib. *Inorg. Chem. Commun.* **2023**, *147*, 110186. [CrossRef]
16. Traoré, N.E.; Berthold, M.; Hartmann, L.; Schmul, P.; Zubiri, B.A.; Spiecker, E.; Peukert, W. Tailoring the Reaction Pathway for Control of Size and Composition of Silver–Gold Alloy Nanoparticles. *J. Phy. Chem. C* **2024**. [CrossRef]
17. Ou, W.; Shen, J.; Lyu, F.; Xiao, X.; Zhou, B.; Lu, J.; Li, Y.Y. Facile Surfactant-, Reductant-, and Ag Salt-free Growth of Ag Nanoparticles with Controllable Size from 35 to 660 nm on Bulk Ag Materials. *Chem. Asian J.* **2021**, *16*, 2249–2252. [CrossRef] [PubMed]
18. Sahadevan, J.; Sojiya, R.; Padmanathan, N.; Kulathuraan, K.; Shalini, M.G.; Sivaprakash, P.; Muthu, S.E. Magnetic property of Fe_2O_3 and Fe_3O_4 nanoparticle prepared by solvothermal process. *Mater. Today Proc.* **2022**, *58*, 895–897. [CrossRef]